



Tailoring transport properties of phase-separated manganite films with ordered magnetic nanostructures

V. Vlaminc, W. Yánez, J. Hoffman, A. Hoffmann, D. Niebieskikwiat

► To cite this version:

V. Vlaminc, W. Yánez, J. Hoffman, A. Hoffmann, D. Niebieskikwiat. Tailoring transport properties of phase-separated manganite films with ordered magnetic nanostructures. *Physical Review B: Condensed matter and materials physics*, American Physical Society, 2016, 94 (6), 10.1103/PhysRevB.94.064404 . hal-02310426

HAL Id: hal-02310426

<https://hal.archives-ouvertes.fr/hal-02310426>

Submitted on 10 Oct 2019

HAL is a multi-disciplinary open access archive for the deposit and dissemination of scientific research documents, whether they are published or not. The documents may come from teaching and research institutions in France or abroad, or from public or private research centers.

L'archive ouverte pluridisciplinaire **HAL**, est destinée au dépôt et à la diffusion de documents scientifiques de niveau recherche, publiés ou non, émanant des établissements d'enseignement et de recherche français ou étrangers, des laboratoires publics ou privés.

Tailoring the transport properties of phase-separated manganite films with ordered magnetic nanostructures

V. Vlaminck,¹ W. Yáñez,¹ J. Hoffman,^{2,3} A. Hoffmann,² and D. Niebieskikwiat¹

¹*Colegio de Ciencias e Ingeniería, Universidad San Francisco de Quito, Quito, Ecuador*

²*Materials Science Division, Argonne National Laboratory, Argonne, Illinois 60439, USA*

³*Department of Physics, Harvard University, Cambridge, MA 02138, USA*

(Dated: July 18, 2016)

Abstract

The magnetotransport properties of thin manganite films ($\text{La}_{0.7}\text{Ca}_{0.3}\text{MnO}_3$) coupled with arrays of permalloy (Py) nanodots deposited on the surface of the film is studied as a function of temperature, magnetic field and size of the dots. In the presence of the magnetic dots, a reduction of the electrical resistivity is observed, especially at the insulator-to-metal transition, as well as a shift of the transition peak towards higher temperature. This indicates that, due to the local interface exchange coupling, highly conductive ferromagnetic domains are nucleated in the manganite film underneath the Py nanodots. The use of a simplified resistor network model allows us to estimate the size of the metallic regions induced by the exchange coupling. At low temperatures, these regions extend ~ 70 nm beyond the edge of the nanodots, a lengthscale comparable to the correlation length of the ferromagnetic clusters in the phase-separated state of $\text{La}_{0.7}\text{Ca}_{0.3}\text{MnO}_3$.

PACS numbers: 75.47.Gk, 71.30.+h, 73.63.-b, 72.80.Ga

Colossal Magnetoresistance (CMR) is a thoroughly studied phenomenon consisting of a large decrease of the electrical resistivity of a magnetic oxide under the influence of moderate magnetic fields.¹⁻⁵ In some manganese perovskites, the so-called manganites, this effect can reach several orders of magnitude, and a strong general consensus indicates that phase separation is a prerequisite for the emergence of these large magnetoresistive effects.³⁻⁵ Phase separation in manganites comprises the coexistence of insulating (paramagnetic or antiferromagnetic) and metallic (ferromagnetic) domains. The relative concentration of these domains determines the electrical properties of the material, with compounds exhibiting CMR on the verge of an insulator-to-metal transition.⁴⁻¹¹ In such a case, an applied magnetic field shifts the balance in favor of the ferromagnetic (FM) phase, concomitantly increasing the conducting volume just enough to produce the well-documented percolative insulator-to-metal transition.⁵⁻¹⁰ Alternatively, similar electrical transitions are usually observed as a function of temperature (T) as well.^{5,8-11}

If any device application is going to be developed from CMR in phase-separated manganites, manipulation of the phase coexistence becomes a central issue to be addressed.^{4,5,12} Although no unique lengthscale has been established for the phase separation, in most cases where CMR occurs the insulating and metallic domains coexist at the submicrometer scale.^{6,7,11,13-17} A prototypical example of CMR based on a percolative insulator-to-metal transition is given by $\text{La}_{0.7}\text{Ca}_{0.3}\text{MnO}_3$ (LCMO), where direct observations show metallic and insulating domains $\sim 100\text{-}200$ nm in size.¹⁷ Therefore, manipulation of the electrical properties necessarily implies the fabrication of different artificial nanostructures.^{5,12,18,19} For example, Ward *et al.* randomly evaporated ferromagnetic Fe nanodots onto a LCMO thin film.¹⁸ According to their results, a large interface exchange coupling of LCMO with the Fe dots pushed the film into a FM phase and induced a percolative transition from the insulating to the metallic state.

In this work, motivated by a controlled manipulation of the transport properties of a phase-separated manganite, we patterned square arrays of permalloy (Py, $\text{Ni}_{80}\text{Fe}_{20}$) nanodots onto the surface of a LCMO thin film. As indicated in Fig. 1(a), the FM nanostructures are expected to favor the formation of ferromagnetic islands in the LCMO film due to a proximity effect, especially in the phase-separated state where the manganite is most sensitive to magnetic perturbations. Since the resistivity in a FM domain is significantly smaller than in the insulating phase, one would expect to modulate the LCMO conductivity depending

on the size of the Py dots and the spacing between them. We present experimental evidence of the enhancement of the conductivity in the LCMO film due to the organized array of magnetic nanodots, and also show how these measurements give the opportunity to study the mechanism and lengthscales involved in the process of the percolative insulator-to-metal transition of manganite films.

A high quality, 20-nm thick $\text{La}_{0.7}\text{Ca}_{0.3}\text{MnO}_3$ film was grown on a LaAlO_3 (100) single crystal at 690°C and an O_3 partial pressure of 2×10^{-6} Torr by ozone-assisted molecular beam epitaxy (MBE). A brief (~ 30 sec) annealing period followed the deposition of each unit cell layer. Film crystallinity was monitored *in situ* using reflection high energy electron diffraction, and after growth the film was characterized by x-ray diffraction, which reveals single-crystalline growth. The c-axis lattice constant is 3.954 \AA , slightly larger than the bulk value (3.86 \AA) and consistent with a small ($\sim 1.8 \%$) compressive in-plane strain from the substrate. Using e-beam lithography, followed by e-beam evaporation of Py under high vacuum (10^{-8} Torr) and subsequent lift-off, we patterned arrays of $h = 20$ nm-thick Py nanodots on the bare LCMO film. Each device, shown in Fig. 1(c), covers an area of $200 \times 400 \mu\text{m}^2$ of the film. Among the three fabricated devices, the first one, shown in Fig. 1(b), consists of a square array of dots of diameter $\phi = 100$ nm spaced by three times the diameter center to center (spacing $3\phi = 300$ nm). This corresponds to a surface coverage of Py of $\sim 8.7 \%$. The second device is made of dots with a diameter $\phi = 200$ nm and the same Py-covered area of 8.7% (spacing $3\phi = 600$ nm), and the last device is a control sample without any dots. The LCMO current path and four probe connections were patterned using photolithography and liquid nitrogen-cooled Ar^+ ion milling. Finally ohmic contacts were formed by wire bonding to 100 nm-thick Au contact pads.

Transport measurements were performed with the magnetic field (H) applied both in-plane and out-of-plane of the film using a Quantum Design PPMS, as well as a Versalab system with external current source and nanovoltmeter from Keithley Instruments. In Figs. 2(a) and 2(b) we show the modification of the transport properties in the LCMO film due to the presence of the Py dots, with magnetic fields applied perpendicular to the plane of the film. For all three devices, magnetotransport measurements exhibit the usual insulator-to-metal transition upon cooling, represented by a peak in the resistivity (ρ) at ~ 190 K, somewhat lower than in bulk LCMO.^{17,20,21} This peak shifts towards higher temperature when a magnetic field is applied. Similarly, as shown in Fig. 2(c), the presence of the

Py dots also significantly reduces the peak resistivity at the insulator-to-metal transition and shifts it towards higher temperature. At zero field: $(\rho_{\text{peak}}, T_{\text{peak}}) = (76 \text{ m}\Omega \text{ cm}, 186 \text{ K})$ for the device without dots; $(58 \text{ m}\Omega \text{ cm}, 194 \text{ K})$ for the 200 nm dots; and $(51 \text{ m}\Omega \text{ cm}, 196 \text{ K})$ for the 100 nm dots. We draw attention to the fact that such a reduction of resistivity cannot be attributed to a short of the current through the Py dots, as one would expect this spurious effect to remain relatively constant throughout the temperature scale. Namely, the resistivity of Py thin films, which varies only slightly with temperature [$\rho_{\text{Py}}(300 \text{ K}) \sim 30 \mu\Omega \text{ cm}$ and $\rho_{\text{Py}}(15 \text{ K}) \sim 20 \mu\Omega \text{ cm}$, Ref. 22], is at all temperatures two to three orders of magnitude smaller than the resistivity of the LCMO film [$\rho_{\text{LCMO}}(300 \text{ K}) \sim 1.4 \times 10^4 \mu\Omega \text{ cm}$ and $\rho_{\text{LCMO}}(15 \text{ K}) \sim 1.1 \times 10^3 \mu\Omega \text{ cm}$]. Then, for a square array of dots of size ϕ separated by 3ϕ center-to-center, the current shortage should result in a reduction of the resistivities $\rho_{\phi=100\text{nm}}$ and $\rho_{\phi=200\text{nm}}$ independent of T of about one third (in the worst case scenario, as long as $\rho_{\text{Py}} \ll \rho_{\text{LCMO}}$). However, as the inset of Fig. 2(a) shows, the reduction of ρ is clearly temperature dependent: it is large ($\sim 60 \%$) around the insulator-to-metal transition where the burst of the FM volume occurs,^{11,17} but small in the high T paramagnetic phase ($\sim 10 \%$). For example, the resistivity of the device without dots is $\sim 23 \text{ m}\Omega \text{ cm}$ at both 140 K and 265 K. However, the drop of resistivity induced by the 100 nm dots at 140 K is $\sim 15 \text{ m}\Omega \text{ cm}$, while it is a modest 2.4 mΩ cm at 265 K. That is, large FM domains can be promoted by the Py dots when the sample is cooled through the insulator-to-metal transition. Both characteristics, the shift of the resistivity peak towards higher T and the asymmetric enhancement of conductivity, unequivocally indicate that the Py nanodots facilitate the percolation of the FM metallic phase in LCMO by means of a magnetic coupling between the LCMO and the Py.

In order to gain insight into the origin of this magnetic proximity effect, we compared the electrical transport properties of the devices with a magnetic field applied parallel (in-plane) and perpendicular (out-of-plane) to the LCMO film. As shown in Fig. 3, the direction of the applied field affects very minimally the resistivity of the samples. At $\mu_0 H = 2 \text{ T}$ the resistivity with the field in-plane is slightly smaller than with the field out-of-plane, even for the bare LCMO. Thus, this minor effect is likely related to the shape anisotropy of the LCMO film, *i.e.*, we conclude that the magnetic interaction between the dots and the LCMO is independent of the Py nanodots being magnetized parallel or perpendicular to the plane of the LCMO film. This rules out dipolar (magnetostatic) interactions as the source of the

magnetic coupling. Due to the large aspect ratio of the Py dots, $\phi/h=100/20$ and $200/20$, the magnetic flux penetrating the LCMO film due to the stray field of the dots, seen in Fig. 3(b), is much larger in the out-of-plane configuration than for the in-plane case (the demagnetizing factor along the axial direction of the dot is ~ 10 - 20 times larger than for the in-plane directions, Ref. 23). Therefore, for a dipolar coupling between the LCMO and the magnetic dots, a more pronounced reduction of resistivity would be expected when the field is perpendicular to the film. The absence of such anisotropy is then a confirmation that the nature of the magnetic proximity effect is an interface exchange coupling. In their previous work with Fe nanodots on LCMO, Ward *et al.* concluded the same through the analysis of the strength of the magnetic coupling.¹⁸ They argued that the stray field of the nanodots (estimated to be smaller than 2 T) is not enough to drive a transition from the insulating to the metallic state, and suggested that an *equivalent field* associated to the magnetic coupling should be well above 9 T. Indeed, in terms of an equivalent *exchange field* (the so-called *molecular field*), spin exchange couplings emulate high local magnetic fields, typically ~ 30 T.²⁴ Therefore, although complete saturation is hard to achieve in phase-separated manganites with typical laboratory fields, it is reasonable to assume that the magnetic islands in the LCMO underneath the Py dots are fully ferromagnetic.

Up to this point, the proximity effect of the Py nanodots appears somewhat equivalent to the application of an external magnetic field. However, this equivalence is only qualitative and far from complete. As shown in the inset of Fig. 2(a), the reduction of resistivity is more pronounced for the 100 nm-dots device than with the dots of 200 nm. In particular, in that figure we show that adjusting the external field at 1.2 T for the device without dots reproduces fairly well the resistivity of the 100 nm Py dots device at zero field. One could argue that this would be an *equivalent field* that results from the spacial average over the LCMO area of the local *exchange fields* of the discrete Py nanodots. However, for the 200 nm-dots device this *equivalent field* drops to ~ 0.84 T, *i.e.*, the smaller Py dots have a larger magnetic influence on the LCMO film. In principle, for the same area of Py ($\sim 8.7\%$) one would expect to have the same FM volume induced in the LCMO in both devices. However, the results shown in Fig. 2 point toward a higher increase of the metallic volume in the LCMO film when the size of the Py dots is reduced. Thus, we propose a scenario where the exchange interaction induces ferromagnetism in the LCMO film in a region that is not sharply delimited by the edge of the Py dots, but it extends a

certain length λ beyond the perimeter of the dots, as sketched in Fig. 1(a). In this way, the effective area of FM islands induced by the Py is proportional to $(1 + 2\lambda/\phi)^2$, thus, it is larger for the smaller dots, supporting the observed results. With the goal to estimate the value of λ we propose a simple phenomenological model, shown in Figs. 4(a) and 4(b), that corresponds to a 2D periodic resistor network. In this model, we assume that a fully-FM domain of small resistivity ρ_F extends over a characteristic length λ outside the Py dots (or inside, if $\lambda < 0$). The remaining volume of LCMO is not simply insulating, but comprises a mixture of conducting and insulating clusters (the unaltered phase-separated state). The resistivity in these regions, ρ_N , is taken equal to the resistivity of the bare LCMO film. With these considerations, the resistivity ρ_ϕ of a given device is reduced to a matrix of resistance elements that are only a function of the resistivities ρ_F and ρ_N , the density of dots, and one fitting parameter, λ . We consider a square lattice of metallic islands with lattice parameter s ($s = 3\phi$ in our case), according to the pattern in Fig. 4(a). In Fig. 4(b) we present the equivalent resistor network, from which we calculate the resistance for the columns with metallic islands (R_1) and for the columns in between, with no islands (R_2);

$$\frac{1}{R_1} = \left[\frac{1}{R_{cell}} + \frac{t(s-D)}{\rho_N D} \right] \frac{\ell}{s} \quad (1)$$

$$R_2 = \frac{\rho_N(s-D)}{t\ell} \quad (2)$$

where $t = 20$ nm is the thickness of the LCMO film and $\ell = 200$ μm is the total width of the device. R_{cell} is the resistance of a square cell of side $D = (\phi + 2\lambda)$ concentric with the circular FM domain of diameter $D = (\phi + 2\lambda)$. The two columns are connected in series and the pattern repeats over the whole length of the device ($L = 400$ μm), such that the total resistance is given by $R_\phi = (R_1 + R_2)L/s$. In this way, the resistivity of the device, $\rho_\phi = R_\phi t\ell/L$, results to be

$$\rho_\phi = \frac{R_{cell} \rho_N (\phi + 2\lambda) t}{\rho_N (\phi + 2\lambda) + t(s - \phi - 2\lambda) R_{cell}} + \frac{\rho_N (s - \phi - 2\lambda)}{s} \quad (3)$$

For the calculation of R_{cell} , we consider a circle of diameter D and resistivity ρ_F immersed within a square of side D and resistivity ρ_N in the corners around the circle, as seen in Fig. 4(a). After the appropriate integration, we found

$$\frac{1}{R_{cell}} = \frac{t}{\rho_N - \rho_F} \left\{ \frac{\rho_N}{\sqrt{\rho_N^2 - (\rho_N - \rho_F)^2}} \tan^{-1} \left(\frac{\rho_N - \rho_F}{\sqrt{\rho_N^2 - (\rho_N - \rho_F)^2}} \right) - \frac{\pi}{2} \left(1 - \frac{\rho_N}{\sqrt{\rho_N^2 - (\rho_N - \rho_F)^2}} \right) \right\} \quad (4)$$

The value of $\rho_N(T, H)$ is taken from the measured resistivity of the sample without dots. However, in order to have λ as the only fitting parameter, an estimate must be made for $\rho_F(T)$. At this point, it is important to consider that the steep increase of resistivity at ~ 150 K is not due to an intrinsic temperature dependence of ρ , but is driven by a drastic reduction of the metallic volume, which is the essence of the insulator-to-metal transition in LCMO.^{10,11,17} Actually, the resistivity of the FM metallic phase remains very small, following a power-law temperature dependence^{3,20,25-27}

$$\rho_F \approx \rho_0(1 + \alpha T^2) + m T^{4.5} \quad (5)$$

where the term $T^{4.5}$ accounts for the electron-magnon scattering²⁸ and the T^2 dependence is usually ascribed to electron-electron interactions.^{3,20,25-27} Indeed, as seen in Fig. 4(c) the resistivity of our LCMO film at $T < 100$ K also follows this law. The coefficient m rapidly decreases with increasing magnetic field. Therefore, since ρ_F in Eq. (4) corresponds to saturated FM domains under the influence of large *exchange fields*, where magnon scattering is largely suppressed, we will neglect the $T^{4.5}$ contribution in $\rho_F(T)$. For the T^2 term we obtained $\alpha = 75 \times 10^{-6} \text{ K}^{-2}$ independent of field, very close to previous results.²⁵ Finally, previous reports have shown that the T -independent term ρ_0 reaches a small saturation value of $\approx 0.1 \text{ m}\Omega \text{ cm}$ ^{3,25,26} (indeed, our LCMO film under a moderate field $\mu_0 H = 4 \text{ T}$ reaches $\rho_0 \sim 0.3 \text{ m}\Omega \text{ cm}$, and for the device with 100 nm dots under the same field ρ_0 drops below $0.2 \text{ m}\Omega \text{ cm}$).

The T dependence of the size of the FM domains ($D = \phi + 2\lambda$), estimated from solving Eqs. (3) and (4) for different applied fields is shown in Fig. 5. We first notice that for high temperatures the Py dots only produce a minor effect on the LCMO film, nucleating FM metallic domains of $\sim 80 \text{ nm}$, even smaller than the diameter of the magnetic dots. This is explained considering that at high T the paramagnetic insulating phase dominates and magnetic perturbations have little effect on LCMO. As a result, the resistivity of LCMO displays only a marginal decrease of around 10 % [inset of Fig. 2(a)]. When the temperature is reduced to $\sim 210 \text{ K}$, the nucleated FM domains rapidly grow in size and start to extend

outside of the limits of the Py dots ($D > \phi$). This growth correlates with a sudden decrease of resistivity in the devices with 100 nm and 200 nm dots [see inset of Fig. 2(a)], indicating that the growth of the FM islands helps to percolate metallic paths throughout the LCMO. For T below ~ 120 K the size of the FM domains reaches field-independent values of $D \sim 220$ nm (for $\phi = 100$ nm) and $D \sim 375$ nm (for $\phi = 200$ nm), *i.e.*, $\lambda \sim 60$ nm and ~ 90 nm for the two devices, respectively. These values, together with the characteristic steep increase of λ at the insulator-to-metal transition (see Fig. 5), suggest that this parameter plays a similar role to a magnetic correlation length. That is, a fully-FM domain is created immediately below the Py dot under the influence of a large *exchange field*, and then these FM correlations propagate up to a characteristic distance λ away from the region of the magnetic perturbation where spins in LCMO directly couple with the spins of the Py. In this context, the value of 2λ should be comparable to the typical size of the FM domains in the bare LCMO, *i.e.*, the typical lengthscale where FM correlations are preserved.⁵ Remarkably, our finding of $2\lambda \sim 120$ -180 nm coincides with direct observations in LCMO, where FM clusters of ~ 100 -200 nm in size were reported.¹⁷

We note that the estimate of the size of the FM islands is always smaller than 3ϕ , the lattice parameter of the square array of Py dots. Thus, the induced FM domains are not large enough to develop percolative paths by themselves. Notwithstanding this, the FM islands do provide percolation paths for the disordered FM clusters that are present in the phase-separated, inter-island regions of LCMO. The consequence of this is that the insulator-to-metal transition occurs at a higher temperature than for the bare LCMO. On the other hand, while for $\phi = 200$ nm the width of the inter-island regions is $3\phi - D \sim 220$ nm, in the 100 nm-dots device they are only ~ 80 nm wide. Moreover, the correction factor for the area coverage of FM islands, $(1 + 2\lambda/\phi)^2$, is ~ 3.5 for the larger Py dots and ~ 4.8 for the smaller ones. These large differences in the topography of the FM islands now quantitatively explain the larger magnetic proximity effect when the LCMO film is covered with smaller Py dots, even though the density of magnetic material deposited is the same.

It is worth noting that the model proposed is a simple phenomenological description of the landscape of magnetic domains and conductivities in the LCMO film under the influence of the Py nanodots, and more detailed models may be developed. For example, FM correlation lengths are defined in the context of the exponential decay of spin-spin correlations at distance r , $e^{-r/\lambda}$. Then, instead of using steep walls at the limits of the FM domains

of diameter $D = \phi + 2\lambda$, a gradient of conductivities may provide a more realistic image of the transport mechanism. Also, the slight difference in the estimate of λ for the devices with 100 nm and 200 nm dots suggests that the growth of the FM islands is probably less organized than in our simple model of well-defined resistance elements. On the other hand, the curiously large value of D at zero field around 140 K is most likely a spurious effect. This may be due to the spin-dependent scattering caused by the misaligned magnetization directions of FM clusters, which contributes to the zero-field resistivity of the phase-separated state. In spite of these details, we showed that our model captures the essential physics of phase-separated manganites and their percolative transport, and provides a new step toward its possible manipulation.

In conclusion, we demonstrated the existence of a substantial exchange coupling between an array of permalloy nanodots and a $\text{La}_{0.7}\text{Ca}_{0.3}\text{MnO}_3$ thin film, which behaves qualitatively similar to the application of a homogeneous magnetic field in the sense that it shifts the insulator-to-metal transition to higher temperatures and significantly reduces the resistivity of the manganite (more than 60 % at its maximum effect). However, this exchange coupling has a local character, and promotes a higher conductivity state on a lengthscale that extends ~ 70 nm beyond the border of the magnetic dots. This lengthscale is determined by the correlation length of the short-range ordered, phase-separated manganite, thus it is comparable to the size of the FM clusters in this state. Our results open the possibility of tailoring the transport properties of manganite films by controlling the characteristics of the deposited ferromagnetic nanostructured lattices, such as their shape, density and lattice parameters.

We thank Leo Ocola for his guidance with the fabrication process and Stephen Wu for helping with the cold Ar-milling. Work at Argonne by JH and AH (including LCMO growth, assistance with sample design and fabrication, and manuscript preparation) was supported by the U.S. Department of Energy, Office of Science, Basic Energy Sciences, Materials Science and Engineering Division. The use of facilities at the Center for Nanoscale Materials, of Office of Science user facility, was supported by the U.S. Department of Energy, Basic Energy Sciences under Contract No. DE-AC02-06CH11357. This work was supported in part by TWAS (grant No. 08-146 RG/PHYS/LA) and the USFQ's Chancellor Grants

program.

-
- ¹ “Colossal Magnetoresistive Oxides”, Advances in Condensed Matter Science series, edited by Y. Tokura, Gordon and Breach Science Publishers (Amsterdam, 2000).
- ² Y. Tokura and Y. Tomioka, *J. Magn. Magn. Mater.* **200**, 1 (1999).
- ³ M.B. Salamon and M. Jaime, *Rev. Mod. Phys.* **73**, 583 (2001).
- ⁴ E. Dagotto, T. Hotta, and A. Moreo, *Phys. Rep.* **344**, 1 (2001).
- ⁵ “Nanoscale Phase Separation and Colossal Magnetoresistance”, E. Dagotto, Springer Series in Solid-State Sciences, Springer (Berlin, 2003).
- ⁶ M. Uehara *et al.*, *Nature (London)* **399**, 560 (1999).
- ⁷ D. Saurel *et al.*, *Phys. Rev. B* **73**, 094438 (2006).
- ⁸ D. Niebieskikwiat *et al.*, *Phys. Rev. B* **66**, 134422 (2002).
- ⁹ V. Hardy, A. Wahl, and C. Martin, *Phys. Rev. B* **64**, 064402 (2001).
- ¹⁰ M. Mayr *et al.*, *Phys. Rev. Lett.* **86**, 135 (2001).
- ¹¹ L. Zhang *et al.*, *Science* **298**, 805 (2002).
- ¹² L. Liang *et al.*, *Nanoscale Res. Lett.* **9**, 325 (2014).
- ¹³ P.G. Radaelli *et al.*, *Phys. Rev. B* **63**, 172419 (2001).
- ¹⁴ A.M. Balagurov *et al.*, *Phys. Rev. B* **64**, 024420 (2001).
- ¹⁵ S. Mori, C.H. Chen, and S.-W. Cheong, *Phys. Rev. Lett.* **81**, 3972 (1998).
- ¹⁶ S. Mori *et al.*, *Phys. Rev. B* **67**, 012403 (2003).
- ¹⁷ M. Fäth *et al.*, *Science* **285**, 1540 (1999).
- ¹⁸ T.Z. Ward *et al.*, *Phys. Rev. Lett.* **106**, 157207 (2011).
- ¹⁹ K. Zhang *et al.*, *Proc. Natl. Acad. Sci. USA* **112**, 9558 (2015).
- ²⁰ M.B. Salamon and S.H. Chun, *Phys. Rev. B* **68**, 014411 (2003).
- ²¹ R. Mahendiran *et al.*, *Phys. Rev. B* **53**, 3348 (1996).
- ²² G. Counil *et al.*, *IEEE Trans. Magn.* **42**, 3323 (2006); M. Haidar and M. Bailleul, *Phys. Rev. B* **88**, 054417 (2013).
- ²³ “Magnetism and Magnetic Materials”, J.M.D. Coey, Cambridge University Press (Cambridge, 2010).
- ²⁴ For a typical FM oxide with a Curie temperature $T_c \sim 200$ K, the nearest neighbour exchange

interaction is $JS^2 \sim 5$ meV, which translates into an effective molecular field $\mu_0 H_{eff} \sim 30$ T. See for example Ref. 23, and also “Introduction to Magnetism and Magnetic Materials”, 2nd Edition, D. Jiles, Chapman & Hall/CRC (Boca Raton, 1998).

²⁵ G.J. Snyder *et al.*, Phys. Rev. B **53**, 14434 (1996).

²⁶ M. Jaime *et al.*, Phys. Rev. B **60**, 1028 (1999).

²⁷ P. Schiffer *et al.*, Phys. Rev. Lett. **75**, 3336 (1995).

²⁸ K. Kubo and N. Ohata, J. Phys. Soc. Jpn. **33**, 21 (1972).

FIGURE CAPTIONS

FIG 1: (a) Schematic of the FM islands induced in the LCMO by the Py dots. λ is the characteristic length where these FM domains extend beyond the limits of the dots. (b) Scanning electron microscopy image of the 100 nm-dots device. (c) Optical microscopy image of the sample with three devices: 100 and 200 nm dots and bare LCMO (no dot).

FIG 2: (a) Resistivity vs temperature for the no-dot device at different fields (as labeled), as well as for the 100 and 200 nm-dots devices at zero field. The black dashed lines closely reproducing the 100 nm (200 nm) device data correspond to the no-dot resistivity measured with applied fields of 1.2 T (0.84 T). Inset: ratio of the resistivity of the devices with 100 and 200 nm Py dots to the resistivity of the bare LCMO film. (b) Resistivity $\rho_\phi(T)$ at different fields (as labeled) for the devices with Py dots of diameters $\phi = 100$ nm and 200 nm. (c) Value of the peak resistivity showing the effect of both perturbations, the external magnetic field and the arrays of FM nanodots.

FIG 3: (a) Comparison of the resistivity between in-plane and out-of-plane external fields of 2 T for the 100 nm and no-dot devices. (b) Illustration of the magnetic flux dispersed from the Py dot for in-plane and out-of-plane configurations.

FIG 4: (a) Square lattice, with lattice parameter 3ϕ , of fully-FM metallic domains of diameter $\phi + 2\lambda$ and resistivity ρ_F , within the phase-separated matrix of resistivity ρ_N . (b) Equivalent two-dimensional resistor network of the pattern shown on the left. R_{cell} is the resistance of the square cell shown in (a), with the circular FM domain inside. R_1 is the

effective resistance of a column containing stacked cells and phase-separated regions, while R_2 is the resistance of the columns in between, with no cells and resistivity ρ_N . (c) Low temperature resistivity of the bare LCMO film at different fields. The solid lines are fits with the power-law dependence of Eq. (5) (see text). The lower line corresponds to the resistivity ρ_F of the saturated FM islands under the Py dots, used in the calculations in Eq. (4).

FIG 5: Temperature dependence of the size of the FM islands that nucleate in LCMO under the Py nanodots, at fields of 0 T, 2 T and 4 T. Solid (open) symbols correspond to the 100 nm (200 nm) diameter Py dots.

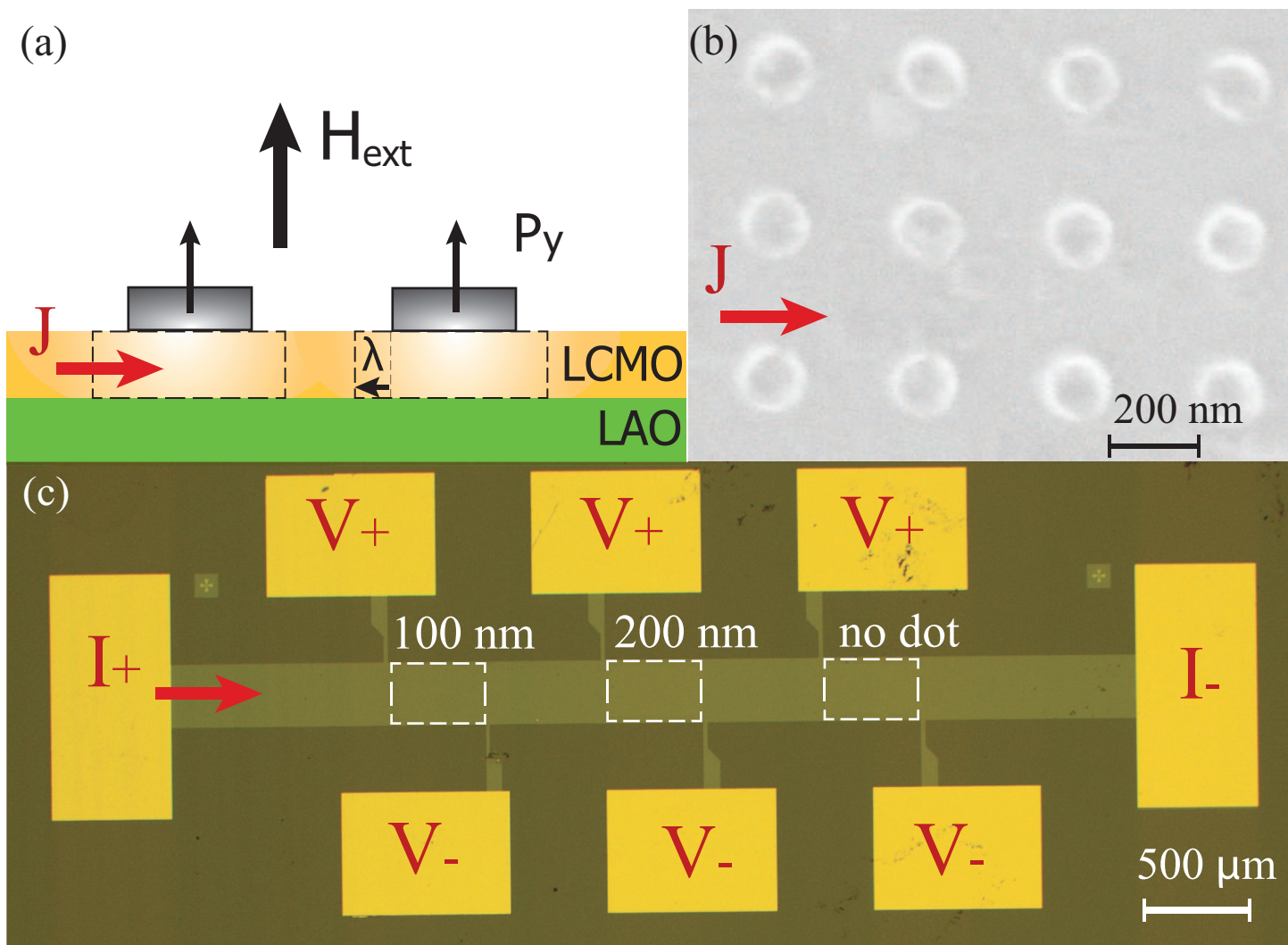


Figure 1

17JUL16

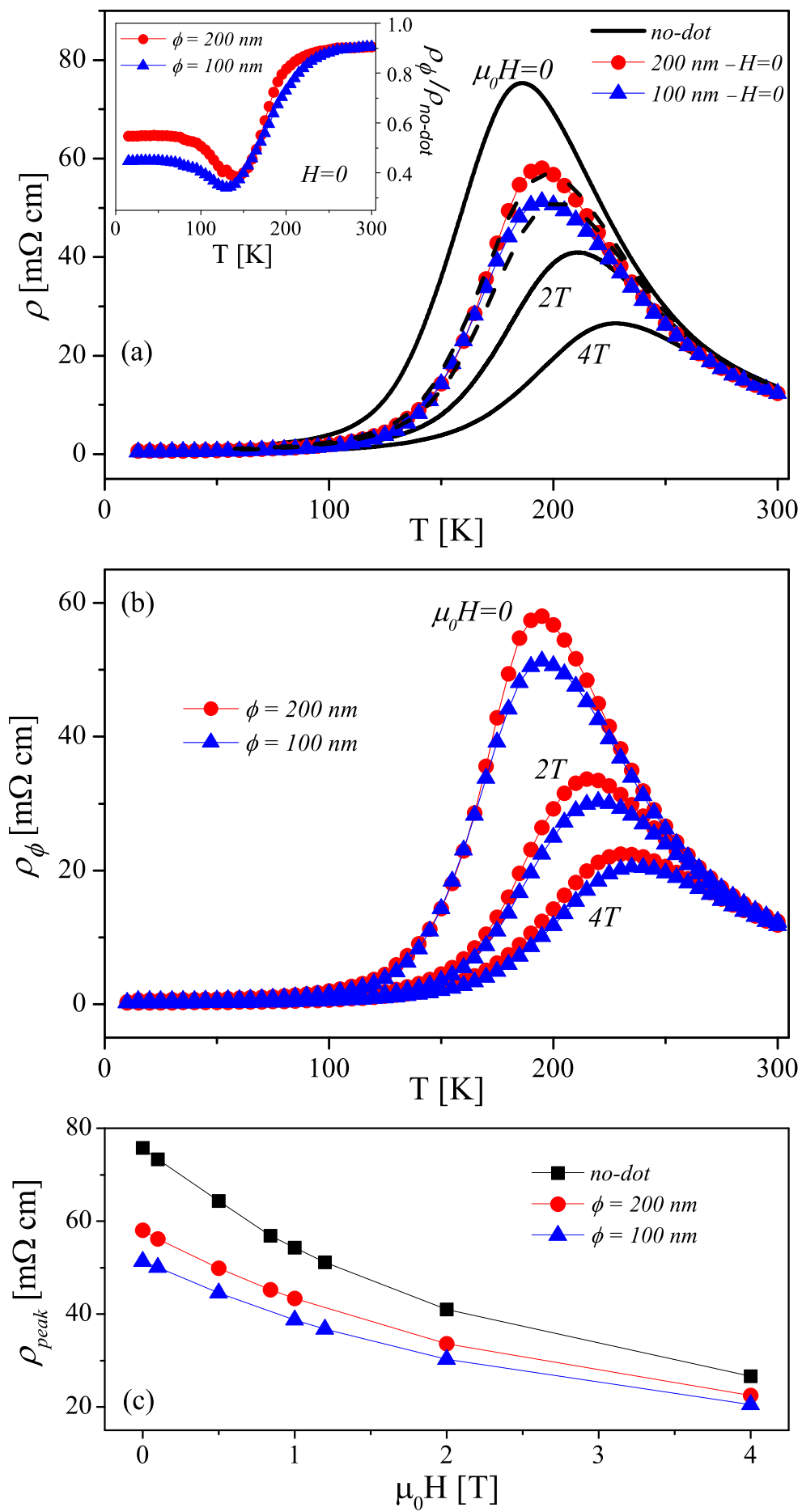


Figure 2

17JUL16

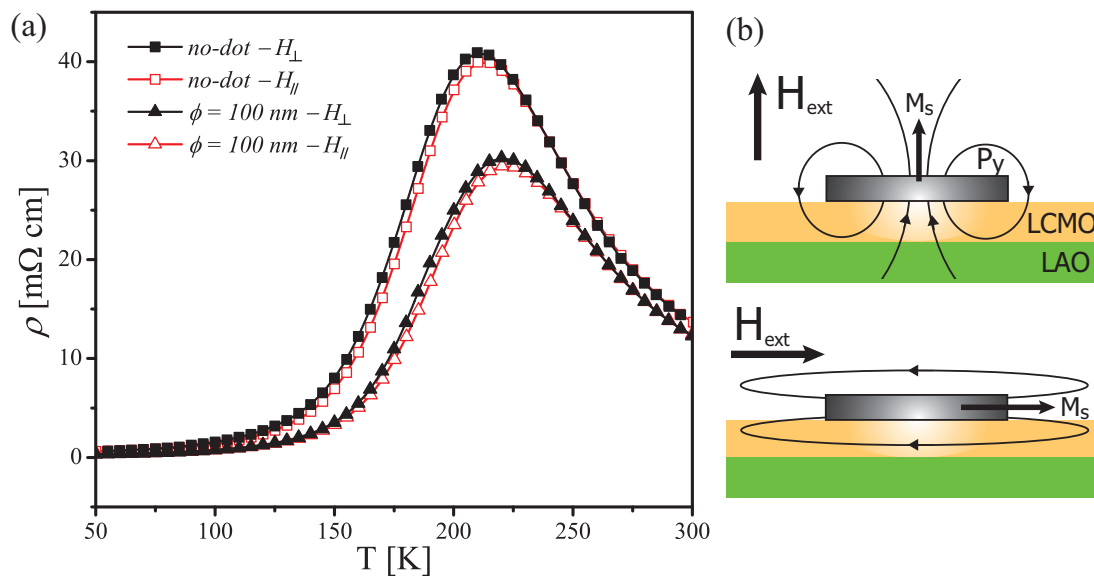


Figure 3

17JUL16

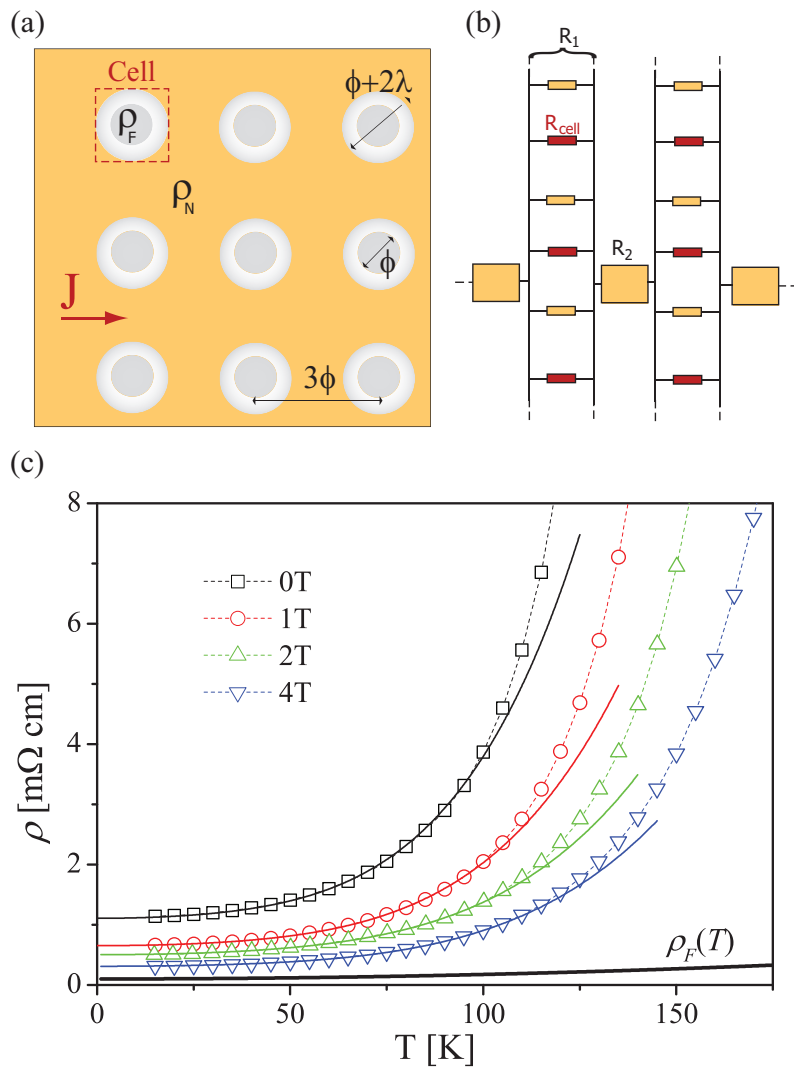


Figure 4

17JUL16

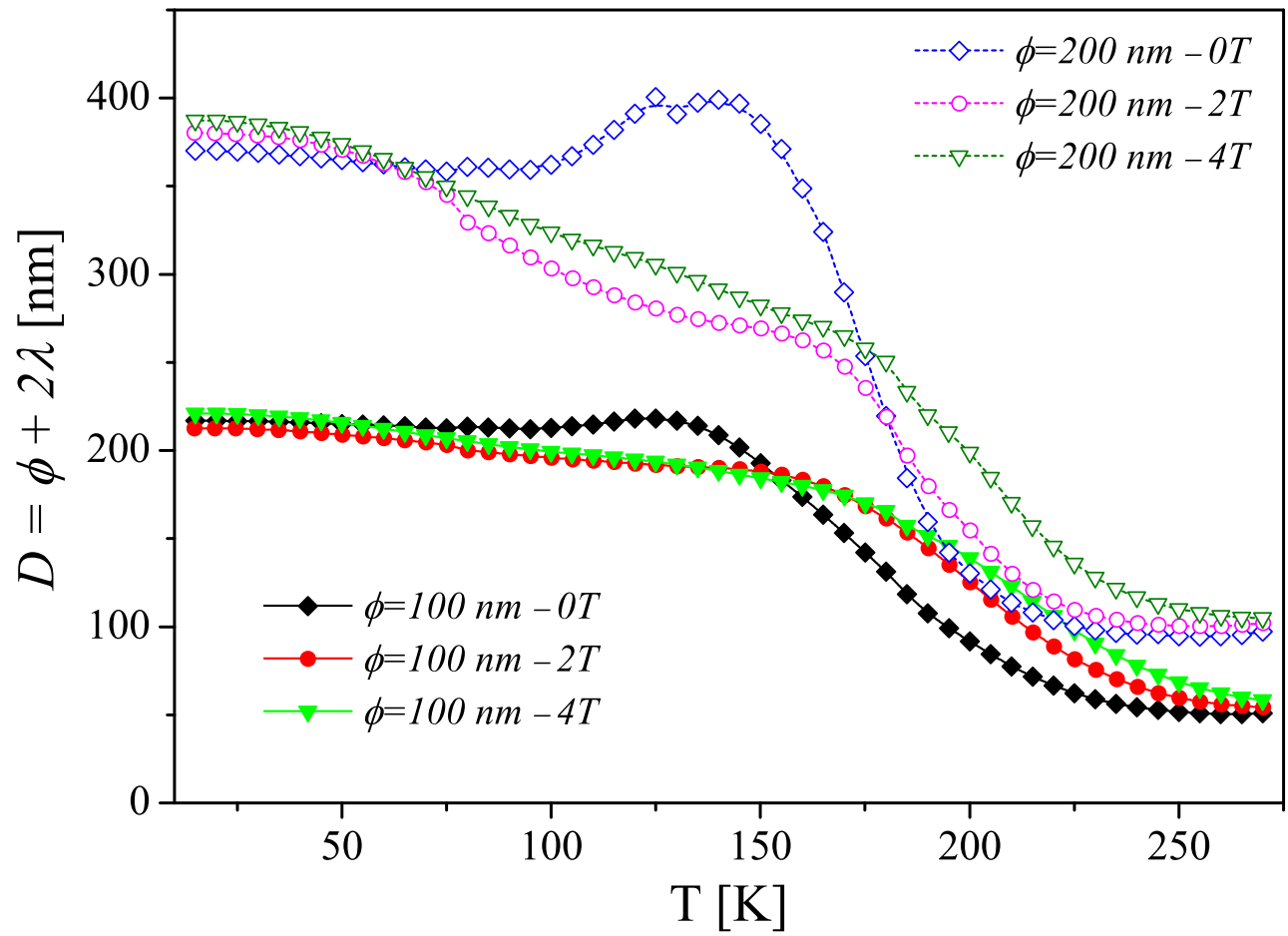


Figure 5

17JUL16